Journal of the Mechanics and Physics of Solids 134 (2020) 103775

Contents lists available at ScienceDirect

Journal of the Mechanics and Physics of Solids

journal homepage: www.elsevier.com/locate/jmps

Type IV failure in weldment of creep resistant ferritic alloys: II. Creep fracture and lifetime prediction ☆

Wei Zhang [a,b], Xue Wang [a], Yiyu Wang [b], Xinghua Yu [b], Yanfei Gao [a,*], Zhili Feng [b,*]

[a] Department of Materials Science and Engineering, University of Tennessee, Knoxville, TN 37996, USA
[b] Materials Science and Technology Division, Oak Ridge National Laboratory, Oak Ridge, TN 37831, USA

ARTICLE INFO

Article history:
Received 25 April 2019
Revised 28 October 2019
Accepted 30 October 2019
Available online 31 October 2019

Keywords:
Type IV failure
Creep strength enhanced ferritic steel weldments
Microstructure-informed and micromechanics-based model
Creep lifetime prediction

ABSTRACT

The creep rupture behavior (Type IV failure) for weldments of creep strength enhanced ferritic steel is numerically analyzed, using an integrated microstructure- and micromechanics-based finite element model. To account for the large microstructure gradients across weldments, a two-dimensional digital microstructure is constructed based on the actual observed microstructure of ferritic steel weldment by using the Voronoi-tessellation method. According to the fracture mechanism studies and literature experimental observations, the Type IV failure is identified as an intergranular creep fracture in the fine-grained or intercritical heated affected zone (FGHAZ or ICHAZ). In the present study, the following micromechanics model is employed to determine the micromechanical and microstructural origins for the failure process above, accounting for the underlying physical fracture mechanisms at different length scales, including nucleation of grain boundary cavities, their growth by competition of grain boundary diffusion and grain interior creep, viscous grain boundary sliding, and the emergence of microcracks by coalescence and their evolution to the ultimate failure. The methodology demonstrates the capabilities in modeling the Type IV failure and providing quantitative creep rupture lifetime prediction which shows an excellent agreement with long-term creep experimental data for creep strength enhanced ferritic steels and their weldments. In particular, the drop-off in time to rupture at high temperatures and low stress levels in the creep rupture curves is quantitatively predicted, and the transition of failure mechanisms from creep-controlled to diffusion-controlled creep fracture mechanism is illustrated.

1. Introduction

Type IV failure, occurring in the intercritical heat affected zone (ICHAZ) or the fine-grained heat affected zone (FGHAZ), has been identified as the primary failure mode of welded structures at high temperatures. The microstructure and material property gradients created by the arc welding thermal cycles has been highlighted as the key drivers of creep

* Corresponding authors.
E-mail addresses: ygao7@utk.edu (Y. Gao), fengz@ornl.gov (Z. Feng).

https://doi.org/10.1016/j.jmps.2019.103775
0022-5096/

cavitation and crack formation in the heat affected zone (HAZ) (Yu et al., 2013a; Abe and Tabuchi, 2004; Gaffard et al., 2005; Watanabe et al., 2006), such as the low hardness, fine grains, and the coarse precipitates in the HAZ. Based on the SEM observations (Abe and Tabuchi, 2004; Kumar et al., 2016; Zhang et al., 2015; Albert et al., 2004; Tabuchi et al., 2001), the Type IV failure has been recognized as creep fracture along grain boundaries, with cavities preferentially nucleating at the interfaces between matrix and coarse precipitates, such as $M_{23}C_6$ (M = Fe, Cr) and Fe_2(W, Mo) Laves phase, or at triple junctions in the ICHAZ or FGHAZ. The failure at high temperatures involves damage activities at a wide range of length scales. Besides cavity nucleation, there are cavity growth under the combined influence of different mechanisms, such as grain boundary diffusion, grain boundary sliding as well as dislocation creep inside grains, microcracking by coalescence of the cavities after sufficient growth along grain boundaries, and the development of macroscopic crack by linking up the microcracks. From a material design point of view, it is important to know how the physical mechanisms and their interactions affect the creep fracture behavior. Thus, there is a requirement to account for the effects of microstructure and the underlying microstructure-dependent deformation and failure mechanisms, in order to investigate the microstructure and micromechanical origin for the Type IV failure.

Finite element methods have been extensively proposed to model the creep flow and damage behavior of the Type IV failure. Firstly, the finite element models with emphasis on the creep deformation of the CSEF steel welds have been developed (Abe and Tabuchi, 2004; Gaffard et al., 2005; Watanabe et al., 2006; Eggeler et al., 1994; Shinozaki and Kuroki, 2003; Yaguchi et al., 2010). These studies generally predict the crack initiation based on the strain accumulation and stress multiaxiality distribution, whereas most of them are not capable of elucidating and simulating the creep damage processes. Secondly, the continuum damage models, incorporating damage by means of micromechanism-based or phenomenological internal variables, have also been utilized for modeling the creep and damage behavior of ferritic steel weldments (Hayhurst et al., 2005; Petry and Gariboldi, 2010; Masse and Lejeail, 2013; Hyde et al., 2010a, 2010b; Zhao et al., 2012a). Hayhurst et al. (2005) simulated the entire creep stages with damage accumulation and analyzed the rupture time using a modified Kachanov-Rabotnov continuum damage model. Hyde et al. (2010) analyzed the creep crack growth behavior of a pre-existing crack in P91 steel welds based on the Liu-Murakami model (Liu and Murakami, 1998). Although the continuum damage models have been used to analyze the rupture life and creep crack growth, they cannot shed lights on the underlying deformation and damage mechanisms which are responsible for the Type IV failure. Nor can they incorporate a faithful representation of the microstructural information. Thirdly, the uncoupled creep fracture mechanics and damage models have been employed to simulate the creep crack growth behavior in the ferritic steel weldments (Yatomi and Tabuchi, 2010; Zhao et al., 2012b). The creep ductility exhaustion approach was adopted to investigate the creep damage accumulation, and the stress and strain rate fields near the crack tip are described by the parameter C^*, which is a path independent integral of the energy release rate. The general idea is to identify the appropriate loading parameter C^*, so that the measured crack growth rates can be transferred from the computational modeling to the experimental measurements. In the above studies, the stress and strain fields near the crack tip are independent of creep damage, that is, the creep rate cannot be accelerated by the damage evolution, which is not the fact in realistic conditions. The above damage models have been employed to study the creep crack growth in CSEF steel weldments, however, they cannot address the actual failure mechanisms and the discreteness of fracture near the crack tips, such as cavity nucleation, growth and coalescence, which are responsible for the creep fracture at high temperatures. Moreover, the service lifetime of CSEF steel weldments depends more on the early stage damage such as cavity nucleation and growth rather than on the crack growth at the later stage (Wang et al., 2018; Smith et al., 2003). It is essential to understand the micromechanics for creep cavitation in order to study the Type IV failure and to provide a reliable remaining life prediction for the weldments of CSEF steels.

The current work aims to adopt a micromechanical constitutive model to systematically study the creep fracture behavior for the Type IV failure, and especially to establish the correlation between the cavity evolution and the creep rupture life in CSEF steel welded joints. The remaining of the paper is organized as follows. A brief review of the assumptions and constitutive laws for the intergranular creep fracture model is presented in Section 2. In contrast to numerous Type IV failure models, our work explicitly calculates the evolution of cavity nucleation and growth in a polycrystalline microstructure. Section 3 discusses the derivation of tangential stiffness matrix and numerical implementation of grain boundary elements, as well as the material parameters used for the computational model. A two-dimensional digital microstructure model with large grain size gradients is constructed to represent the heterogeneous microstructure of welded joints, and application and validation of the model to represent the creep failure response of CSEF steel weldments is reported in Section 4. The concluding remarks are given in Section 5.

2. Constitutive models

According to the fracture mechanism map (Gandhi and Ashby, 1983), a material typically exhibits three types of fracture modes in the creep regime: intergranular creep fracture, transgranular creep fracture, and rupture. Rupture only takes place at extremely high temperatures ($> 0.8T_m$, where T_m is the melting temperature). For structural material used around 50% of their melting temperature, the transgranular and intergranular creep fracture due to cavity coalescence are important mechanisms under such creep conditions. The former usually happens at high stress (short term creep fracture) and the latter dominates at lower stress (long term creep fracture). Type IV failure, happening at high temperature and low stress conditions (~ 600 °C and 100 MPa or less), belongs to the intergranular creep fracture. Microstructure examinations also confirmed the Type IV failure occur at grain boundaries, with the preferential nucleation sites for creep voids being the

grain boundary particles associated with inclusions or second phase particles (Abe and Tabuchi, 2004; Watanabe et al., 2006; Kumar et al., 2016; Albert et al., 2004; Tabuchi et al., 2001; Besson et al., 2009). Therefore, the following micromechanism-based intergranular creep fracture model (Tvergaard, 1984a, 1984b; Onck and Van Der Giessen, 1998; Onck and van der Giessen, 1998) is employed to simulate and investigate the micromechanical origin for the Type IV failure.

A pioneer work of the creep fracture model was proposed by Hull and Rimmer (1959) concerning the growth of one single cavity by grain boundary diffusion. Then the modeling of cavity growth was modified by Needleman and Rice (Needleman and Rice, 1983), in which the contribution of the creep deformation to the cavity growth was incorporated and its coupling with grain boundary diffusion was studied. The grain boundary cavity nucleation law and a smeared-out representation of discrete cavity distribution on grain boundaries was proposed (Tvergaard, 1984b; Van Der Giessen and Tvergaard, 1994). Onck and van der Giessen combined the cavity growth model with the cavity nucleation law, which has been employed to simulate the intergranular creep fracture behavior of various polycrystalline materials (Onck and Van Der Giessen, 1998; Onck and van der Giessen, 1997; Onck and Van der Giessen, 1998; Yu et al., 2012; Yu et al., 2013b; Yu et al., 2014). The constitutive description involves physics for the Type IV cracking at different length scales, i.e., grain boundary cavity nucleation and growth, viscous grain boundary sliding, microcracking by the coalescence of cavities, and microcracks link up to form macroscopic cracks finally leading to premature failure. In this present work, a user-defined element (UEL) subroutine and a user-defined material (UMAT) subroutine are utilized to implement the rate-dependent cohesive behavior of the grain boundary and the creep deformation of the grain interior, respectively, into the commercial finite element software, ABAQUS (Abaqus, 2012). The constitutive equations of the micromechanics model are summarized as followings.

2.1. Creep model

The material inside the grains is assumed to be deformed by dislocation (power-law) creep in addition to the elastic deformation, and the total strain rate is the sum of elastic and creep strain rate,

$$\dot{\varepsilon}_{ij} = \dot{\varepsilon}^{e}_{ij} + \dot{\varepsilon}^{p}_{ij} \ . \tag{1}$$

These two components can be obtained from

$$\dot{\varepsilon}^{e}_{ij} = \frac{1+\nu}{E}\left(\dot{\sigma}_{ij} - \frac{\nu}{1+\nu}\dot{\sigma}_{kk}\delta_{ij}\right), \tag{2}$$

$$\dot{\varepsilon}^{p}_{ij} = A_{dis}\frac{EbD_l}{k_B T}\left(\frac{\sigma_e}{\sigma_0}\right)^n \frac{3S_{ij}}{2\sigma_e}\cdot \bar{M}^I, \tag{3}$$

where E and ν are Young's modulus and Poisson's ration, respectively; δ_{ij} is the Kronecker delta; k_B is the Boltzmann's constant; b is the Burgers vector; T is the absolute temperature; $\sigma_e = \sqrt{3S_{ij}S_{ij}/2}$ is the von Mises stress; n is the stress exponent; σ_0 is the reference stress; A_{dis} is the material constant; D_l is the diffusivity coefficient for the dislocation creep $D_l = D_{0l}\exp(-Q_l/RT)$; $\bar{M}^I$ is the normalized micromechanical Taylor factor (Raabe et al., 2001) for the I_{th} grain, $\bar{M}^I = M^I/\max(M^1, M^2, \ldots, M^I, \ldots, M^{N_g})$, N_g is the total number of grains within the polycrystalline model. The micromechanical Taylor factor (Raabe et al., 2001) is introduced to represent the slip anisotropy induced by crystallographic orientation of each individual grain, and it is defined as the ration between the local accumulated shear $\Sigma\gamma^{local}$ and the local von Mises strain $\langle\varepsilon^{local}_{VM}\rangle$, $M = \sum\gamma^{local}/\langle\varepsilon^{local}_{VM}\rangle$, where $\Sigma\gamma^{local}$ and $\langle\varepsilon^{local}_{VM}\rangle$ are numerically calculated by using a modified crystal plasticity model (Huang, 1991) . During deformation, dislocation creep strain percolation follows grains which are geometrically soft and avoids grains those are hard.

In our companion paper (Part I), the Coble creep is incorporated into the constitutive law. However, this mechanism is now integrated into the cavity growth process, as will be shown shortly, so that the Coble deformation mechanism is not needed explicitly.

2.2. Grain boundary cavitation

The creep cavitation process at grain boundaries involves the nucleation, growth, and coalescence of cavities. The cavities on a grain boundary are characterized by the spherical-caps shape with radius a, half-spacing b, and cavity tip angle ψ, as shown in Fig. 1(a). During cavity growth the cavity tip angle ψ keeps a constant value of about 75° (Onck and van der Giessen, 1997). The cavity volume V is computed as

$$V = \frac{4}{3}\pi a^3 h(\psi), \tag{4}$$

where h is the spherical-caps shape parameter,

$$h(\psi) = \frac{\left[(1+\cos\psi)^{-1} - 1/2\cos\psi\right]}{\sin\ \psi}. \tag{5}$$

It is difficult to explicitly model each individual cavity on grain boundaries, and therefore a smeared-out representation of grain boundary cavities (Rice, 1981) is introduced to simplify the problem, in which the discrete distribution of cavities

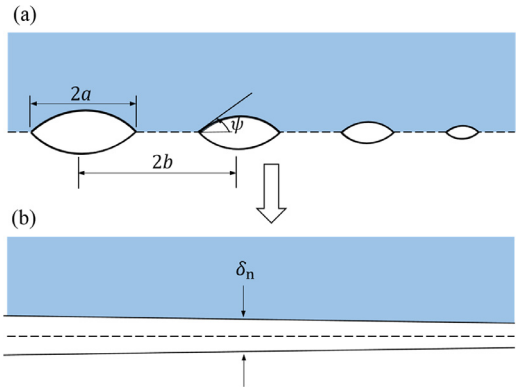

Fig. 1. Schematic plots for (a) geometry of spherical shape cavities located at grain boundaries and (b) the smeared-out representation of grain boundary cavitation in terms of a continuous varying separation δ_n.

on each grain boundary is replaced by a continuous varying separation $u_n = V/(\pi b^2)$, as shown in Fig. 1(b). The rate of normal separation varies continuously,

$$\dot{u}_n = \frac{\dot{V}}{\pi b^2} - \frac{2V\dot{b}}{\pi b^3}, \tag{6}$$

which is determined by the volumetric growth rate $\dot{V}$ (Section 3.4), and the rate of change of the cavity spacing $\dot{b}$ (Section 3.3).

2.3. Cavity nucleation

The nucleation of cavities during high temperature deformation is a complex process that takes place at the very small length scales. Experiment observations show that density of cavities increases in proportion to the creep strain and it highly depends on the grain boundary microstructure, such as the distribution of second-phase particles or segregation impurities (Abe and Tabuchi, 2004; Watanabe et al., 2006; Albert et al., 2004; Tabuchi et al., 2001). Due to the complexity of the nucleation process and lack of detailed experimental measurements, the physical description of cavity nucleation is not readily available. In the present work, a phenomenological model proposed by Tvergaard (Tvergaard, 1984b) is adopted, in which the cavity nucleation rate is a function of the effective creep rate $\dot{\varepsilon}_e^c$ and normal stress σ_n near the grain boundary,

$$\dot{N} = F_n\left(\frac{\sigma_n}{\Sigma_0}\right)^2 \dot{\varepsilon}_e^c \text{ for } \sigma_n > 0, \tag{7}$$

where Σ_0 is a reference stress, F_n is the material parameter that incorporates the microstructural features that influence cavity nucleation rate at a grain boundary, and $\dot{\varepsilon}_e^c = \dot{\varepsilon}_0(\sigma_e/\sigma_0)^n$, where $\dot{\varepsilon}_0 = A_{dis}\frac{EbD_l}{k_B T}$. It has been shown from experiments that nucleation of cavities on some grain boundaries only occurs in the late stage of creep life (Abaqus, 2012), i.e., there exists a threshold before the cavity nucleation takes place. To account for the threshold, a parameter that combines the stress and strain accumulation has been proposed (Onck and van der Giessen, 1998),

$$S = \left(\frac{\sigma_n}{\Sigma_0}\right)^2 \varepsilon_e^c \text{ for } \sigma_n > 0. \tag{8}$$

The cavity nucleation can be triggered only when the parameter S reaches a threshold value S_{thr}, which is defined in terms of the initial cavity density N_i as

$$S_{thr} = \frac{N_i}{F_n}. \tag{9}$$

With continuous cavity nucleation on grain boundaries, the cavity spacing decreases and the changing rate is determined by

$$\frac{\dot{b}}{b} = \frac{1}{2}(\dot{\varepsilon}_I + \dot{\varepsilon}_{II}) - \frac{1}{2}\frac{\dot{N}}{N}, \tag{10}$$

where $\dot{\varepsilon}_I$ and $\dot{\varepsilon}_{II}$ are in-plane principle logarithmic strain rate at the grain boundary and N is the cavity density, which is defined as the number of cavities per unit undeformed grain boundary.

2.4. Cavity growth

The cavities grow by both the diffusion of atoms from their surface into the grain boundary layer and also the creep deformation of the surrounding grains. The cavity growth relations in the present work are based on the pioneering work of Needleman and Rice (Needleman and Rice, 1983). The volumetric cavity growth rate $\dot{V}$ can be expressed as

$$\dot{V} = \dot{V}_1 + \dot{V}_2, \tag{11}$$

where $\dot{V}_1$ is the contribution of grain boundary diffusion, given by

$$\dot{V}_1 = 4\pi D \frac{\sigma_n - (1-f)\sigma_s}{\ln(1/f) - \frac{1}{2}(3-f)(1-f)}, \tag{12}$$

and $\dot{V}_2$ represents the cavity growth induced by creep deformation,

$$\dot{V}_2 = \begin{cases} \pm 2\pi \dot{\varepsilon}_e^c a^3 h(\psi)\left[\alpha_n \left|\frac{\sigma_m}{\sigma_e}\right| + \beta_n\right]^n, & \text{for } \pm\frac{\sigma_m}{\sigma_e} > 1 \\ 2\pi \dot{\varepsilon}_e^c a^3 h(\psi)[\alpha_n + \beta_n]^n \frac{\sigma_m}{\sigma_e}, & \text{for } \left|\frac{\sigma_m}{\sigma_e}\right| < 1 \end{cases}, \tag{13}$$

where σ_s is the sintering stress, which is usually small and can be neglected, $\alpha_n = 3/(2n)$, and $\beta_n = (n-1)(n+0.4319)/n^2$. In Eq. (12), f is the effective cavity volume fraction given by

$$f = \max\left[\left(\frac{a}{b}\right)^2, \left(\frac{a}{a+1.5L}\right)^2\right], \tag{14}$$

where L dictates the coupling of diffusion and creep deformation to the cavity growth and it is described through a stress and temperature dependent length scale

$$L = \left[D\frac{\sigma_e}{\dot{\varepsilon}_e^c}\right]^{1/3}, \tag{15}$$

D is the grain boundary diffusion parameter and defined by

$$D = \frac{D_{b0}\delta_b\Omega}{k_B T}\exp\left(-\frac{Q_b}{RT}\right), \tag{16}$$

where $D_{b0}\delta_b$ is the diffusion coefficient of grain boundary, Q_b is the activation energy of grain boundary diffusion, and Ω is the atom volume. The cavity growth rate can be calculated from the cavity volume change

$$\dot{a} = \dot{V}/\left(4\pi a^2 h(\psi)\right). \tag{17}$$

2.5. Grain boundary sliding

Grain boundary sliding (GBS) is one of the competing mechanisms that contribute to the creep deformation and damage of ferritic steel weldments (Abe et al., 2008; Kimmins and Smith, 1998). GBS is a thermally activated process driven by shear tractions acting tangentially to the grain boundary and is be governed by Newtonian viscous flow,

$$\dot{u}_t = \frac{\Omega\eta_0 \exp\left(-Q_{gbs}/RT\right)}{k_B T}\sigma_t \tag{18}$$

where η_0 is a characteristic sliding velocity, Q_{gbs} is the activation energy for grain boundary sliding, and $\dot{u}_t$ is the relative sliding velocity of adjacent grains due to the shear stress σ_t.

3. Numerical simulation

3.1. Numerical implementation

Under high temperature and low stress loading conditions, deformation and damage behavior of CSEF steels and their weldments usually results from both the creep deformation within grains and grain boundary activities, including GBS and grain boundary cavitation. In the present study, a user-defined material (UMAT) subroutine is implemented into ABAQUS (Abaqus, 2012) to simulate the elastic deformation and the dislocation creep within grain interiors. Also, a rate-dependent cohesive element is developed to model the grain boundary cavitation and GBS by implementing a user-defined element subroutine (UEL) in ABAQUS (Abaqus, 2012). The derivation of the tangent stiffness matrix for the cohesive element is described below.

The grain boundaries in a creeping material may separate when there is stress concentration or sufficiently accumulated strain. In the present study, the grain boundary interfacial behavior is described by the cohesive laws that relate the normal and tangential tractions with the corresponding displacements. In the normal direction, the traction vs. separation relation is governed by the constitutive laws of creep cavitation, including cavity nucleation, growth and their coalescence on grain

boundaries. Substituting Eq. (7), (10), (12), (13) into Eq. (6) yields the normal separation rate as a function of the normal traction,

$$\dot{u}_{\mathrm{n}} = A\sigma_{\mathrm{n}}{}^2 + B\sigma_{\mathrm{n}} + C, \tag{19}$$

where

$$A = \frac{V}{\pi b^2}\frac{1}{N}\frac{F_{\mathrm{n}}}{\Sigma_0^2}\dot{\varepsilon}_{\mathrm{e}}^{\mathrm{c}}, \tag{20a}$$

$$B = \frac{1}{\pi b^2}\frac{4\pi D}{\ln(1/f) - \frac{1}{2}(3-f)(1-f)}, \tag{20b}$$

$$C = \frac{\dot{V}_2}{\pi b^2} - \frac{V}{\pi b^2}(\dot{\varepsilon}_{\mathrm{I}} + \dot{\varepsilon}_{\mathrm{II}}). \tag{20c}$$

The three terms on the right side of Eq. (19) represent contributions of cavity nucleation, grain boundary diffusion and the creep deformation to the total normal separation of the grain boundary.

The partial derivative of the normal incremental stress with respect to the normal incremental displacement is derived from Eq. (19),

$$\frac{\partial \Delta\sigma_{\mathrm{n}}}{\partial \Delta u_{\mathrm{n}}} = \frac{1}{(2A\sigma_{\mathrm{n}} + B)\Delta t}\ . \tag{21}$$

In the tangential direction, the relationship between the shear stress and tangential displacement obeys the Newtonian viscous flow, as presented in Eq. (20). The partial derivative of the incremental shear stress with respect to the incremental tangential displacement is

$$\frac{\partial \Delta\tau}{\partial \Delta u_{\mathrm{t}}} = \frac{kT}{\Omega\eta_0 \exp\left(-Q_{\mathrm{gbs}}/RT\right)}\frac{1}{\Delta t}, \tag{22}$$

where, Δt is the time increment.

Combining Eq. (23) with Eq. (24), the material Jacobian matrix is obtained as

$$\begin{Bmatrix} \Delta\sigma_{\mathrm{n}} \\ \Delta\tau \end{Bmatrix} = \begin{bmatrix} \frac{1}{(2A\sigma_{\mathrm{n}}+B)\Delta t} & 0 \\ 0 & \frac{kT}{\Omega\eta_0 \exp\left(-Q_{\mathrm{gbs}}/RT\right)\Delta t} \end{bmatrix} \begin{Bmatrix} \Delta u_{\mathrm{n}} \\ \Delta u_{\mathrm{s}} \end{Bmatrix} \tag{23}$$

It is worth noting that the normal and tangential separations on the grain boundary are independent as only the diagonal terms exist in the material Jacobian matrix.

Fig. 2 shows a schematic example of the finite element mesh and the role of UMAT and UEL during the solving procedure. For the grain interiors, the plane strain elements (CPE3) are used to simulate the elastic deformation and the dislocation creep. The cohesive elements are added on each grain boundary to connect the facets of adjacent grains during the fracture process. A cohesive element is made up of four nodes, with two of them residing on a grain facet. The corresponding nodes of the cohesive element initially lie together in the unstressed state with zero thickness. The applied load induces both the normal and tangential stresses on the element faces, which in return result in the interface separations according to the above constitutive laws. In order to model the creep fracture behavior, the numerical analysis of the interface elements requires not only the knowledge of the state-dependent variables of the grain boundary elements, but also the variables in the surrounding grains. Therefore, the COMMON BLOCK technique is introduced for data storage and acquiring between UMAT and UEL subroutines, i.e., the information of state variables, including the mises stress σ_{e}, mean stress σ_{m}, and effective creep rate $\dot{\varepsilon}_{\mathrm{e}}^{\mathrm{c}}$, are stored when the UMAT subroutine is called for computing the grain interior deformation, and they will be acquired by UEL subroutine for calculating the creep fracture development of grain boundaries.

3.2. Material parameters

The material parameters for grain interior creep deformation are adopted from our Part I work, as listed in Table 1. The reference stress, stress exponent, and the coefficient for dislocation creep are given by $\sigma_0 = 0.001E$, where E is the Young's modulus at 650 °C (Eggeler et al., 1994), $n = 8$ and $A_{\mathrm{dis}} = 16.0\ \mathrm{s}^{-1}$, respectively. For the grain boundary elements, the values of materials properties are listed in Table 2. Among these parameters, the reference stress Σ_0 in the nucleation law is taken as that suggested by Onck and van der Giessen (1998), the grain boundary viscosity η_0, atomic volume Ω, and the activation energy of grain boundary diffusion Q_{gbs} are taken from literature (Frost and Ashby, 1982; Bower and Wininger, 2004). The initial cavity density and radius are $N_I = 40N_R$ and $a_I = 6.7 \times 10^{-4}\ R_0$, where R_0 is the half facet length $d = 3.64R_0$ and $N_R = 1/\pi R_0^2$, respectively. The cavity half spacing is related with the initial cavity density as $b_I = 1/\sqrt{\pi N_I}R_0 = 0.16R_0$. The sintering stress σ_{s} is usually relatively small and can be neglected. The only unknowns parameters F_{n} and $D_{\mathrm{b0}}\delta_{\mathrm{b}}$ will be determined via calibration with the experimental creep data for Grade 91 steel and its weldments (Yu et al., 2013a; Tabuchi and Takahashi, 2006; Abe, 2016), and in the following they will be specified by dimensionless parameters F_{n}/N_R

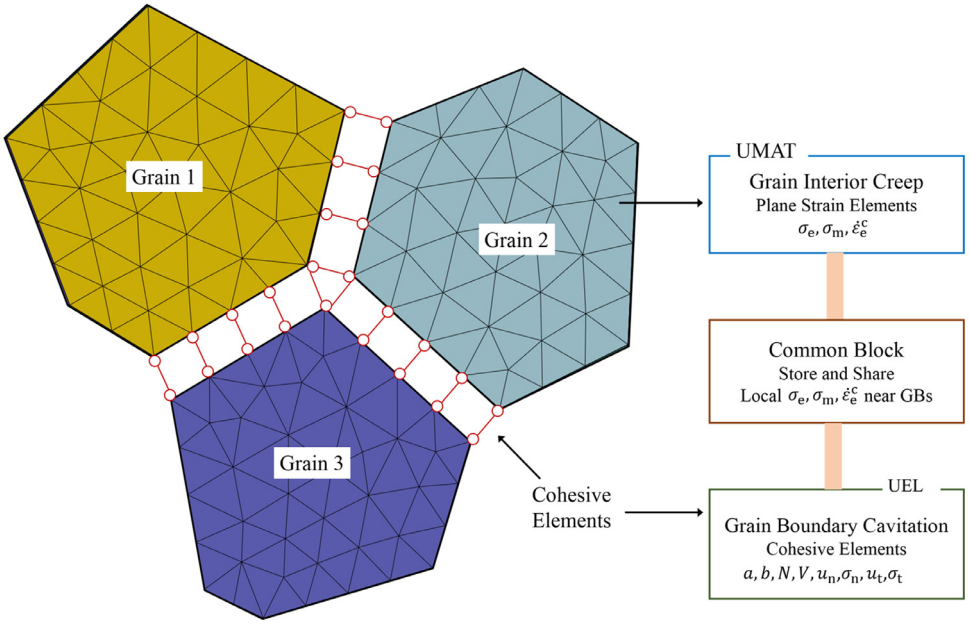

Fig. 2. Schematic illustration of the finite element mesh and the cohesive elements along the grain boundaries. The use of UMAT and UEL subroutines is also depicted.

Table 1
Representative values for material parameters used for dislocation creep within grain interiors.

Parameter	Value
Atomic volume, Ω	1.18×10^{-29} m^3
Melting temperature, T_M	1810 K
Burgers vector, b	2.48×10^{-10} m^3
Young's modulus, E_0	223 GPa
Young's modulus at 650 °C, E	90.14 GPa
Poisson's ratio, ν	0.3
Lattice diffusion pre-exponent, D_{0l}	0.021m^2/s
Lattice diffusion activation energy, Q_l	500KJ/mole
Dislocation creep coefficient, A_{dis}	16.0 s^{-1}
Reference stress, σ_0	90.14 MPa
Stress exponent, n	8

Table 2
Calibrated material parameters for grain boundary constitutive model.

Parameter	Value
Grain boundary diffusion pre-exponent for BM, $(D_{00gb}\delta)_{BM}$	5.317×10^{-20} m^3/s
Grain boundary diffusion pre-exponent for HAZ, $(D_{00gb}\delta)_{HAZ}$	1.139×10^{-19} m^3/s
Cavity nucleation parameter $(F_n/N_R)^{BM}$	9.4248×10^3
Cavity nucleation parameter $(F_n/N_R)^{H-HAZ}$	1.2174×10^4
Cavity nucleation parameter $(F_n/N_R)^{L-HAZ}$	5.027×10^4
Grain boundary diffusion activation energy, Q_{gb}	174KJ/mole
Reference stress, Σ_0	90.14 MPa
Grain boundary sliding pre-exponent, η_0	40m/s
Average grain size in FGHAZ, d	1 μm
Average grain size in the other zones, d	5 μm

and L/R_0, respectively, with L defined as $L = (D\sigma_e/\dot{\varepsilon}_e^c)^{1/3}$. These parameters are crucial in governing the relative contribution of characteristic time scales of nucleation, diffusion, and creep deformation. The dimensionless length L/R_0 indicates the relative contribution of diffusion over creep, while F_n/N_R specifies the nucleation activities. In the following, the competitive mechanisms of the diffusion and creep deformation to fracture behavior for the weldment of Grade 91 steel will be addressed.

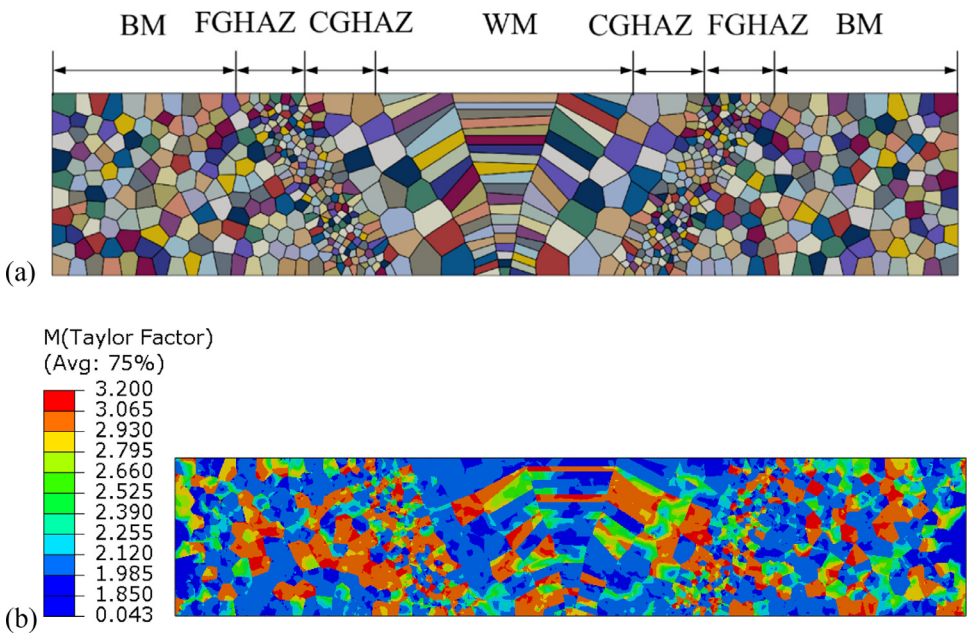

Fig. 3. (a) Two-dimensional digital microstructure model for weldment of creep-resistant steels with grain size gradients in BM, FGHAZ, CGHAZ, and WM. (b) Crystallographic orientation of each individual grain represented by the micromechanical Taylor factor (each grain assigned with random orientations).

4. Results and discussion

To consider the microstructural heterogeneities of ferritic steel weldments, a two-dimensional digital microstructure has been constructed by using Voronoi tessellation method (Tvergaard, 1984b), as shown in Fig. 3. The generated digital microstructure agrees well with experimental sample in its topological and structural properties. The average grain sizes of FGHAZ and the other regions (BM, CGHAZ and WM) are assumed to be 1 μm and 5 μm, respectively. Taking advantage of the digital microstructure, the influences of microstructural heterogeneities (e.g., orientation and shape of all grains, and gradient in the grain size), as well as heterogeneous material properties on the scale of individual grains (e.g., hardness variation and heterogeneous grain boundary diffusivity), will be examined.

4.1. Creep life assessment

The development of Type IV failure involves the nucleation of cavities on grain boundaries, their growth, microcracking by coalescence, and the propagation of microcracks to the formation of macrocrack. Previous experimental investigations (Wang et al., 2018; Smith et al., 2003) have shown the cavity nucleation and growth continue up to the late stage of creep life. Once the microcracks initiate and link up to form macrocracks, the welded joints will break up in a very short time. Therefore, it is crucial to understand the evolution of cavity nucleation and growth behavior so as to provide reliable remaining life prediction for the CSEF steel welded joints. The micromechanics-based model is applied to investigate the creep cavity evolution for the Type IV failure. Fig. 4 summarized the collected creep rupture data based on the fracture locations for the weldments of Grade 91 steel (Tabuchi and Takahashi, 2006). The cross-welds are mainly fractured in the base metal or weld metal at lower temperatures and higher stresses, while the fracture location shifts to the HAZ with increasing temperature or decreasing stress. In particular, for longer term creep, e.g., with rupture life more than 200 h at 650 °C, 900 h at 600 °C and 5000 h 550 °C, the Grade 91 steel welded joints mainly fracture in HAZ, which is the well-known Type IV failure. The slope of stress vs. rupture time curve is expected to change when the fracture location shifts from base metal or weld metal to the heat affected zone, as the fracture mechanism transfers from transgranular fracture to intergranular fracture with decreased stress or increased temperature. Nevertheless, the change of slope is not distinct in Fig. 4, which is due to the large data scatter and lack of long-term rupture data (with life more than 10^4 hours). Such scatter band in the creep rupture data for the heat resistant steel and its welded joints were commonly reported in the literature (Abe, 2016; Kimura and Takahashi, 2012), which can be caused by the difference in the heat treatment conditions, material compositions and welding procedures, etc.

The creep rupture data which are fractured in the HAZ together with those for base material of Grade 91 steel are presented (Abe, 2016; Science, 2014), as shown in Fig. 5, for calibrating the material parameters (F_n/N_R and L/R_0) for both the FGHAZ and base metal. The numerical results for creep rupture life show quantitative agreement with the experimental data (Yu et al., 2013a; Tabuchi and Takahashi, 2006; Abe, 2016; Science, 2014). The black dash and solid lines represent

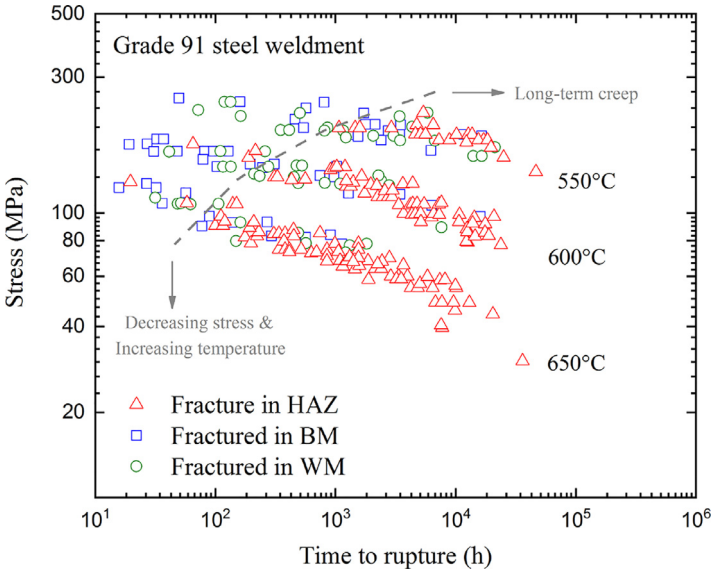

Fig. 4. Double logarithmic plot of applied stress vs. time to rupture in terms of fracture locations (HAZ, BM and WM) for Grade 91 steel weldments (X. Yu et al., 2013; Watanabe et al., 2006; Tabuchi and Takahashi, 2006; Abe, 2016; Tabuchi et al., 2009).

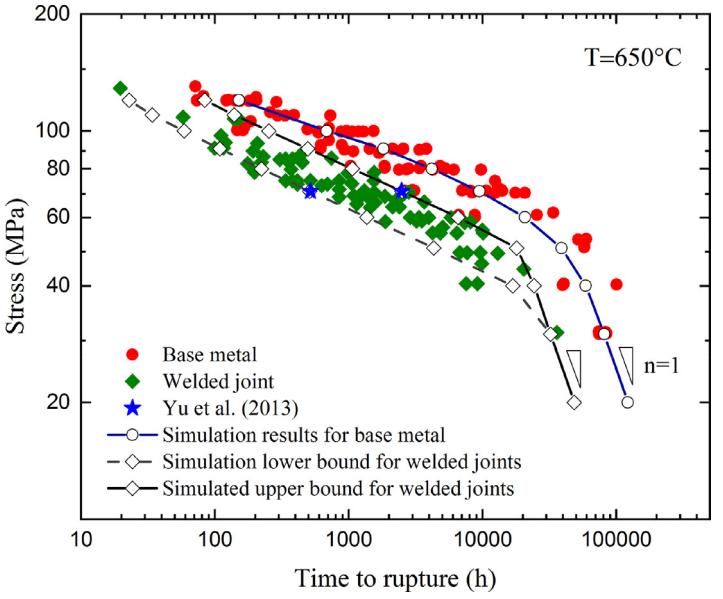

Fig. 5. Stress vs. creep life behavior predicted using the micromechanical model for both the base metal and welded joints of Grade 91 steel in comparison with the literature experimental data (X. Yu et al., 2013; Watanabe et al., 2006; Tabuchi and Takahashi, 2006; Abe, 2016; Science, 2014) at 650 °C.

the simulated lower and upper bounds for the rupture life of welded joints (passing through the creep rupture data by Yu et al. (2013a)), and the blue solid line is the simulated average value of the creep rupture life for the base metal of Grade 91 steel, respectively. The unknown parameters F_n/N_R and L/R_0 for both base metal and FGHAZ are determined as shown in Table 2. It is observed that the reduction of creep rupture time accelerates in the long-term creep region ($>10^4$ hours) for both the base metal and welded joints, which is represented by a steeper slope in the stress vs. rupture life curve. Generally, this sharp slope transition indicates the micromechanics change for intergranular creep fracture, i.e., the competitive activity of cavity nucleation and cavity growth and the transition from creep-controlled to diffusion-controlled creep fracture mechanism. For the long-term creep region (rupture life $>10^4$ hours), it is observed the slope of $\log(\sigma)$-$\log(t_r)$ equals to -1, which implies the rupture time is inversely proportional to the diffusional creep rate ($\dot{\varepsilon} \propto \sigma$). This is consistent with the conclusion of the Hull and Rimmer model (Hull and Rimmer, 1959) that assumes the creep cavitation is controlled by surface and grain boundary diffusion. Under low applied stresses, creep fracture is only controlled by atom diffusion induced cavity growth. The evolution characteristics of creep cavitation will be discussed in the following.

4.2. Evolution of creep cavities

During creep exposure, the cavities grow by both atom diffusion and the creep deformation of neighboring grains, in the meanwhile the cavity number increases with accumulated creep strain, which attests to the enlargement of the existing cavities and nucleation of new cavities (Wang et al., 2018; Smith et al., 2003). As the cavity itself could not support load, the size of isolated cavities keeps growing while the spacing between neighboring cavities decreases. Eventually, the adjacent cavities join together and form microcracks on grain boundaries. The damage state is quantified by the ratio between the cavity size and half-spacing, i.e. a/b. Experiment observations show that the coalescence may occur earlier by ductile tearing or the cleavage of the ligament between the cavities, and here we assume coalescence occur when $a/b = 0.9$. The cavity growth is represented by increase of the cavity radius a, while cavity nucleation is denoted by decrease of the cavity half-spacing b. Fig. 6 and Fig. 7 show the variation of cavity size a, half spacing b and the damage ratio of a/b with the creep life for the FGHAZ of the standard and nonstandard condition corresponding to Yu et al. (2013a). It is observed that rates of both cavity growth and nucleation increase with the applied stress. The cavity half-spacing b and its changing rate decrease with creep time, that is, cavities continuously nucleate and saturate on the grain boundaries, which is consistent with the experiment measurement of cavity nucleation in FGHAZ (Wang et al., 2018). The high applied stress promotes early cavity nucleation and results in large density of cavities on grain boundaries in the welded joints. Moreover, there is no cavity nucleation for a long-term creep at low applied stresses ($<$ ~40 MPa), and only the growth of pre-existing cavities leads to the microcracks and final failure along grain boundaries. The damage variable a/b as a function of creep life is plotted in Figs. 6(c) and 7(c) for the standard and nonstandard condition, respectively. It increases monotonically and reaches the damage value sooner for a higher applied stress, giving rise to a shorter creep rupture life. Compared the creep cavitation of the standard condition with those of the nonstandard condition, there is no significant difference in the growth of cavity size a, while the cavity half-spacing b decreases more rapidly in the standard condition as shown in Fig. 6(b), which is due to the higher cavity nucleation in the FGHAZ and also the higher creep deformation induced by the reduced hardness. At high temperatures, the cavity nucleation is usually related with the large second phase particles on the grain boundaries. The numerical simulation is consistent with the fact that the standard treatment weld with coarse and sparse distribution of $M_{23}C_6$ in the FGHAZ lead to the accelerated cavity nucleation and shortened creep rupture life. The quantitative link between the precipitate distribution and cavity nucleation behavior will be left for our future work.

Fig. 8 shows the numerical results for creep curves in comparison with experiment measurements (Yu et al., 2013a). The creep curves are well predicted for both the standard and nonstandard pre-tempered weldments of Grade 91 steel, with presence of both the secondary creep and the tertiary creep stages. In the secondary creep stage, the creep rate remains constant, which is commonly attributed to the dynamic balance between the strain hardening by dislocation and the softening by microstructure degradation and recovery. At high temperatures and low stresses, creep mainly involves diffusion and hence the recovery rate is high enough to balance out the strain hardening, which results in the appearance of secondary creep. In the tertiary creep stage, due to the prominent effect of damage evolution, the creep rate increases dramatically until the creep rupture happens, As shown in Fig. 6 and Fig. 7, the creep cavities grow fast in the late stage of creep life, and it leads to the rapidly increasing rate of microcraking by coalescence, i.e., damage ratio a/b.

Exactly when numerical simulation stops at failure depends on the mesh size; refining the mesh size leads to large rupture strain. However, this is not of any practical importance, because any fluctuation in material properties may lead to earlier failure than the numerical prediction. A more meaningful definition of the fracture strain, ε_f^*, is given by the strain extrapolated from the steady-state creep at the rupture time, as shown in Fig. 8. This follows the empirical finding of Monkman-Grant relationship, i.e., $\dot{\varepsilon}_{ss} t_r$ is insensitive to the temperature. This modified failure strain ε_f^* is underestimated when compared with the actual creep ductility. However, considering the fact that the crept sample becomes unstable and loses its load carrying capabilities because of the accelerated activities of creep damage, the modified failure strain ε_f^* can be used as an estimate for the loss of creep strength. It is demonstrated that the micromechanics-based computational model processes the capability of modeling the creep strain of welded joints with the evolution of creep damage.

4.3. Type IV cracking

Fig. 9 presents the contour plot of the von Mises stress distribution for the whole weldment of Grade 91 steel under 650 °C and 70 MPa. Type IV failure is successfully simulated by using the micromechanics model. Note that the deformation is enlarged by 10 times for the ease of visualization. Compared with the base metal and weld metal, FGHAZ exhibits the most serious damage across the whole weld, which is due to the accelerated creep cavitation activities. This can be correlated with the following factors. The softened FGHAZ, with a higher dislocation creep deformation, results in earlier cavity nucleation and contributes more to the cavity growth in this region. Meanwhile, the higher boundary to volume fraction in the FGHAZ also provides more sites for cavity formation on grain boundaries or triple junctions due to grain boundary sliding. In addition, the cavity nucleation is more prominent in the FGHAZ as evidenced by the experiment measurements, i.e., the coarse precipitates, such as $M_{23}C_6$ and Laves phases, aggregate at grain boundaries in FGHAZ and provide favorable nucleation sites for creep voids. Due to the stress transfer from the crack tip to its neighbor, the stress concentration is observed in the grains near the crack tip, which probably promotes the creep cavitation and damage on the neighboring grain boundaries.

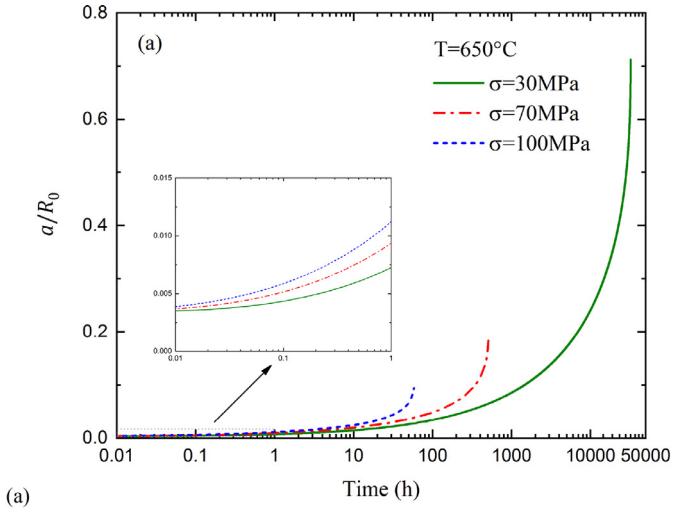

(a)

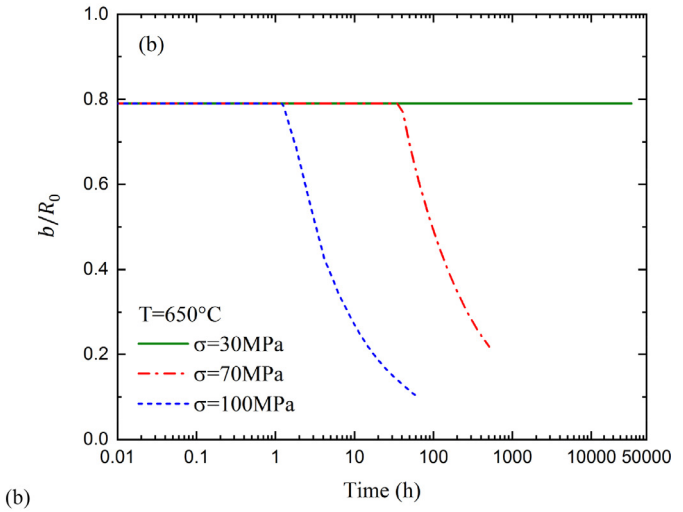

(b)

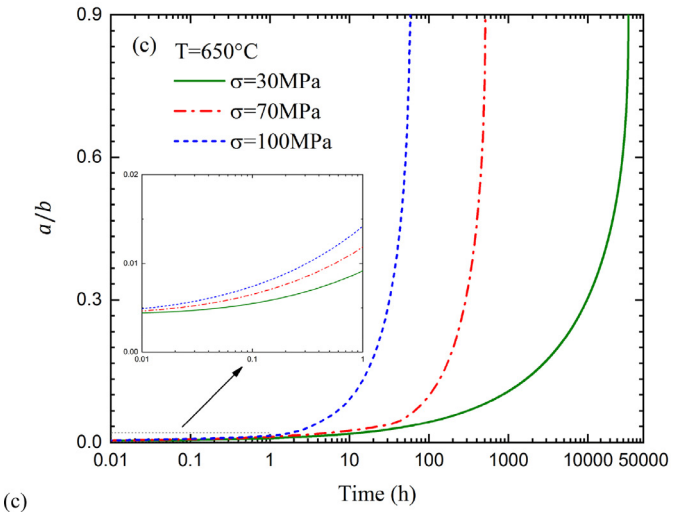

(c)

Fig. 6. Creep cavitation examined by (a) the normalized cavity radius, (b) the normalized half-spacing, and (c) the ratio versus normalized time relationships for nonstandard pre-weld tempered Grade 91 weldment for applied stress of 30, 70, and 100 MPa at 650 °C.

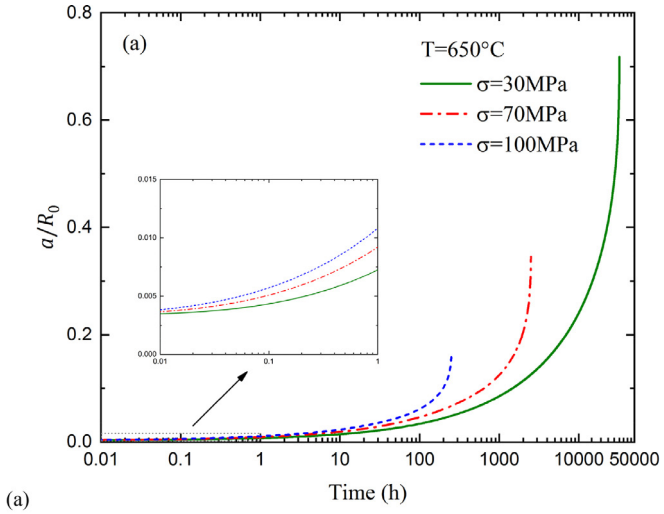

(a)

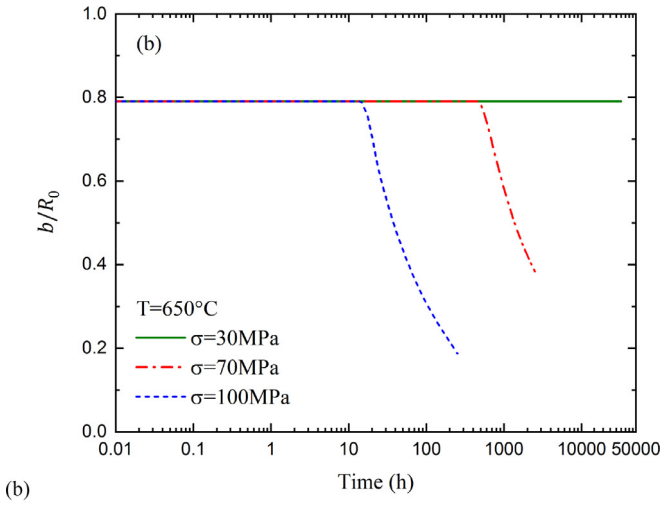

(b)

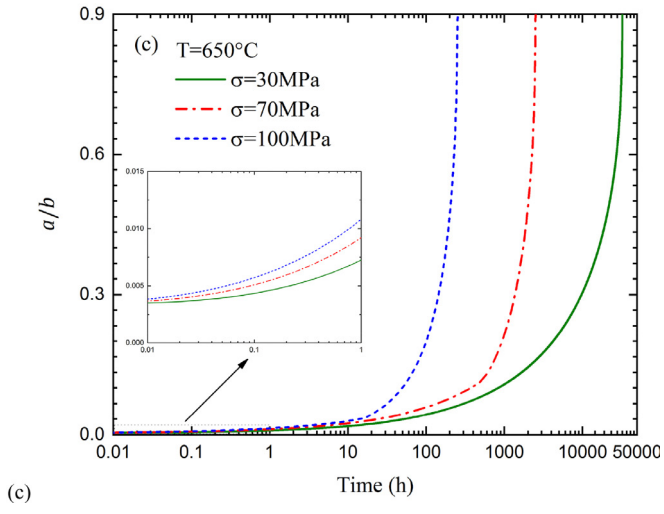

(c)

Fig. 7. Creep cavitation examined by (a) the normalized cavity radius, (b) the normalized half-spacing, and (c) the ratio versus normalized time relationships for standard pre-weld tempered Grade 91 weldment for applied stress of 30, 70, and 100 MPa at 650 °C.

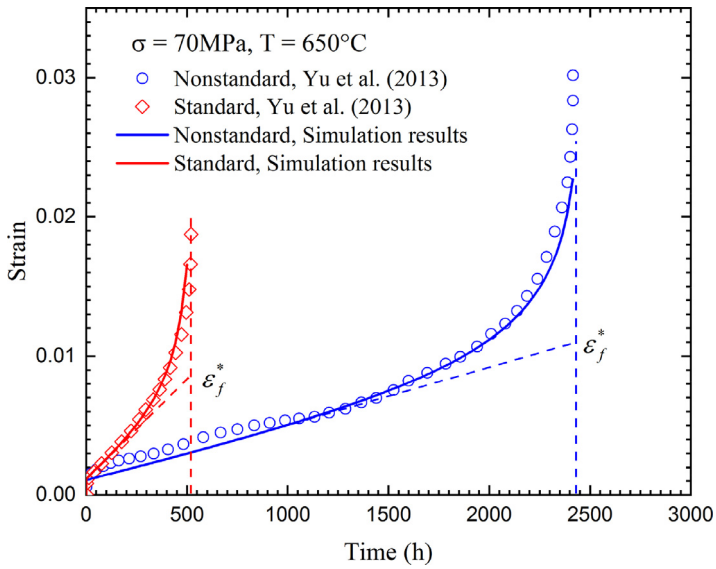

Fig. 8. Comparison of simulated (lines) and experimental (symbols) (X. Yu et al., 2013) creep strain curves for the nonstandard and standard pre-weld tempered Grade 91 steel weldments at 650 °C and 70 MPa.

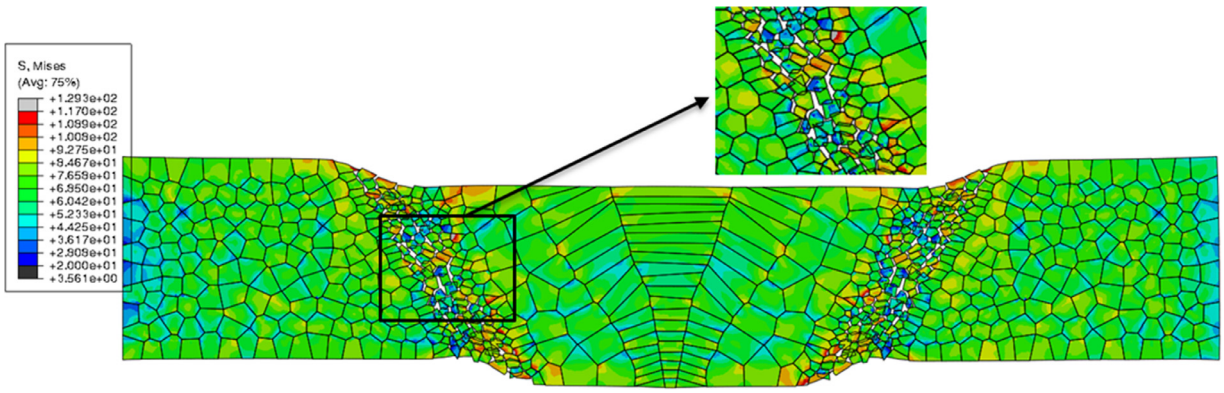

Fig. 9. Contour plot of the von Mises stress distribution in the whole weldment. Type IV cracks take place in the fine-grained HAZ.

Based on the viewpoint of deformation and fracture mechanism, the creep fracture can be categorized into diffusion-controlled and creep-controlled behavior, where the competition of these two can be represented by the dimensionless parameter L/R_0. Fig. 10(a) presents the contour plot of L/R_0 as a function of normalized temperature T/T_M and applied stress σ/E, where T_M is the melting temperature. The large value of L/R_0 implies that grain boundary diffusion dominates the cavity growth, which leads to the relative brittle creep fracture constrained by the grain interior creep at low applied stress and temperature. With the increased temperature, the contribution of both the creep deformation and the grain boundary diffusion becomes higher, but the role of grain interior creep grows faster because of its high activation energy. The value of L/R_0 gradually decreases, that is, the contribution of creep deformation to the fracture behavior becomes more important while increasing the temperature and applied stress. As the schematic fracture mechanism map in Fig. 10(b), it shows a material exhibits several fracture modes depending on the loading conditions, i.e., the temperature and stress. At high temperatures, the creep fracture mechanism often changes from the transgranular creep fracture at high stress (short-term creep) to the intergranular creep fracture at low stress (long-term creep). Based on our numerical study, it is found that the region with intergranular creep fracture can be divided into two subregions, where the creep-controlled region is favored at high applied stresses and temperatures and the diffusion-controlled region is located at relatively low stresses and temperatures. In realistic condition, the Type IV cracking could be influenced by the microstructural evolutions in the late stage of long-term creep exposure, such as the dynamic recovery, recrystallization, and coarsening of precipitates. Though the numerical simulation may not represent the exact cavity evolution during creep exposure, it is captures the main features of experimental observations (Wang et al., 2018; Smith et al., 2003). Incorporating such microstructure changes into the finite element modeling for creep damage will be the interest of our future work.

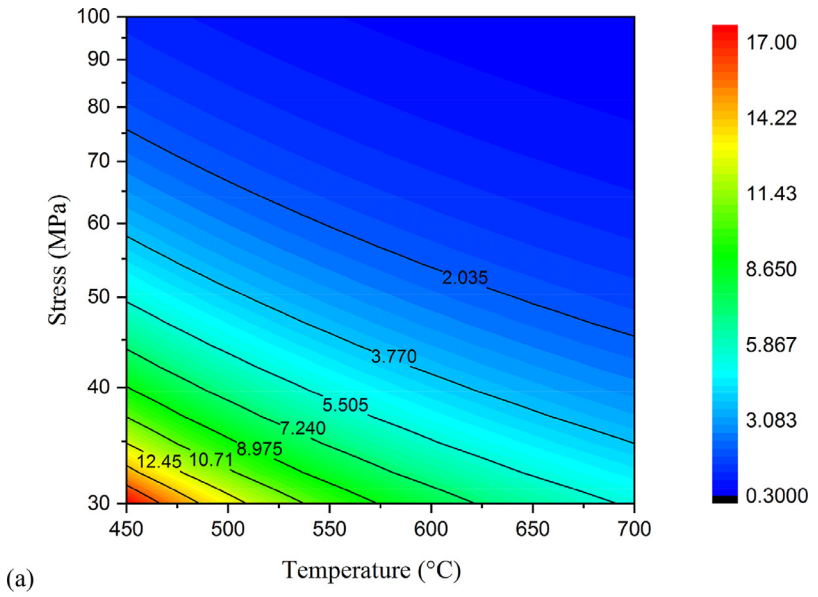

(a)

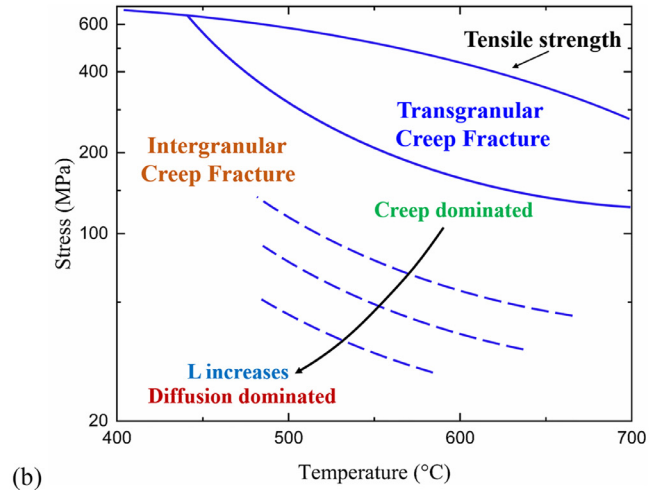

(b)

Fig. 10. (a) Contour plot of the normalized length, L/R_0, which represents the competition of GB diffusion and creep deformation to the cavity growth. (b) Schematic illustration of the transition from creep-dominated to diffusion-dominated intergranular fracture.

5. Conclusions

An integrated microstructure-micromechanics-based finite element model was applied to systematically study creep fracture behavior for the Type IV failure in CSEF steel weldments, in presence of nucleation of creep cavities on grain boundaries, their growth as well as the microcracking by coalescence. By taking advantage of the microstructure-based model, we can explicitly model the weld microstructure and examine the effects of grain scale material heterogeneities, including grain size/ morphology, grain orientation and creep properties of different zones. The numerical results illustrate the creep fracture is a cavity-growth controlled process in the long-term creep rupture region ($> 10^4$ hours) when stress is low, while increasing stress it is a coupled cavity-nucleation and cavity-growth process. From the fracture mechanism point of view, the creep fracture is governed by grain boundary diffusion in long-term creep at low stresses and temperatures, and the contribution of creep deformation becomes more important with increased applied stresses and temperatures. Moreover, the computational model provides a reliable creep life assessment for CSEF steel weldments.

Declaration of Competing Interest

The authors declare no competing interests.

Acknowledgements

The authors are grateful to financial support by the U.S. Department of Energy, Cross-Cutting Materials R&D Program. Additionally, XW acknowledges partial support from the Center for Materials Processing at The University of Tennessee, Knoxville, and YFG acknowledges National Science Foundation DMR 1809640.

Supplementary materials

Supplementary material associated with this article can be found, in the online version, at doi:10.1016/j.jmps.2019.103775.

References

Abaqus, C., 2012. Analysis User's manual, Version 6.12. ABAQUS.
Abe, F., Tabuchi, M., 2004. Microstructure and creep strength of welds in advanced ferritic power plant steels. Sci. Technol. Weld. Join. 9 (1), 22–30.
Abe, F., Kern, T.-.U., Viswanathan, R., 2008. Creep-Resistant Steels. Elsevier.
Abe, F., 2016. Progress in creep-resistant steels for high efficiency coal-fired power plants. J. Press. Vess. Technol. 138 (4), 040804.
Albert, S., Matsui, M., Hongo, H., Watanabe, T., Kubo, K., Tabuchi, M., 2004. Creep rupture properties of HAZs of a high Cr ferritic steel simulated by a weld simulator. Int. J. Pressure Vess. Pip. 81 (3), 221–234.
Besson, J., Leclercq, S., Gaffard, V., Gourgues-Lorenzon, A.-.F., 2009. Analysis of creep lifetime of a ASME grade 91 welded pipe. Eng. Fract. Mech. 76 (10), 1460–1473.
Bower, A.F., Wininger, E., 2004. A two-dimensional finite element method for simulating the constitutive response and microstructure of polycrystals during high temperature plastic deformation. J. Mech. Phys. Solids 52 (6), 1289–1317.
Eggeler, G., Ramteke, A., Coleman, M., Chew, B., Peter, G., Burblies, A., Hald, J., Jefferey, C., Rantala, J., Mohrmann, R., 1994. Analysis of creep in a welded 'P91'pressure vessel. Int. J. Press. Vess. Pip. 60 (3), 237–257.
Frost, H.J., Ashby, M.F., 1982. Deformation Mechanism maps: the Plasticity and Creep of Metals and Ceramics. Pergamon press.
Gaffard, V., Gourgues-Lorenzon, A.-.F., Besson, J., 2005. High temperature creep flow and damage properties of 9Cr1MoNbV steels: base metal and weldment. Nuclear Eng. Des. 235 (24), 2547–2562.
Gandhi, C., Ashby, M. Fracture-mechanism Maps For Materials Which cleave: FCC, BCC and HCP Metals and ceramics, Perspectives in Creep Fracture, Elsevier 1983, pp. 33–70.
Hayhurst, R., Mustata, R., Hayhurst, D., 2005. Creep constitutive equations for parent, type IV, R-HAZ, Cg-HAZ and weld material in the range 565–640 C for Cr–Mo–V weldments. Int. J. Press. Vess. Pip. 82 (2), 137–144.
Huang, Y., 1991. A User-Material Subroutine Incroporating Single Crystal Plasticity in the ABAQUS Finite Element Program. Harvard Univ.
Hull, D., Rimmer, D., 1959. The growth of grain-boundary voids under stress. Philos. Mag. 4 (42), 673–687.
Hyde, T., Saber, M., Sun, W., 2010a. Creep crack growth data and prediction for a P91 weld at 650 C. Int. J. Press. Vess. Pip. 87 (12), 721–729.
Hyde, T., Saber, M., Sun, W., 2010b. Testing and modelling of creep crack growth in compact tension specimens from a P91 weld at 650 c. Eng. Fract. Mech. 77 (15), 2946–2957.
Kimmins, S., Smith, D., 1998. On the relaxation of interface stresses during creep of ferritic steel weldments. J. Strain Anal. Eng. Des. 33 (3), 195–206.
Kimura, K., Takahashi, Y., 2012. Evaluation of long-term creep strength of asme grades 91, 92, and 122 type steels. In: Proceedings of the ASME 2012 Pressure Vessels and Piping Conference. American Society of Mechanical Engineers, pp. 309–316.
Kumar, Y., Venugopal, S., Sasikala, G., Albert, S.K., Bhaduri, A., 2016. Study of creep crack growth in a modified 9Cr–1Mo steel weld metal and heat affected zone. Mater. Sci. Eng. A 655, 300–309.
Liu, Y., Murakami, S., 1998. Damage localization of conventional creep damage models and proposition of a new model for creep damage analysis. JSME Int. J. Ser. A Solid Mech. Mater. Eng. 41 (1), 57–65.
Masse, T., Lejeail, Y., 2013. Creep mechanical behaviour of modified 9Cr1Mo steel weldments: experimental analysis and modelling. Nuclear Eng. Des. 254, 97–110.
Needleman, A., Rice, J., 1983. Plastic Creep Flow Effects in the Diffusive Cavitation of Grain boundaries, Perspectives in Creep Fracture. Elsevier, pp. 107–124.
Onck, P., van der Giessen, E., 1997. Microstructurally-based modelling of intergranular creep fracture using grain elements. Mech. Mater. 26 (2), 109–126.
Onck, P., Van Der Giessen, E., 1998. Micromechanics of creep fracture: simulation of intergranular crack growth. Comput. Mater. Sci. 13 (1–3), 90–102.
Onck, P., van der Giessen, E., 1998. Growth of an initially sharp crack by grain boundary cavitation. J. Mech. Phys. Solids 47 (1), 99–139.
Onck, P., Van der Giessen, E., 1998. Microstructural modelling of creep crack growth from a blunted crack. Int. J. Fract. 92 (4), 373–399.
Petry, C., Gariboldi, E., 2010. Experimental characterisation and modelling of the creep properties of a P92 steel weldment. Mater. High Temp. 27 (1), 1–10.
Raabe, D., Sachtleber, M., Zhao, Z., Roters, F., Zaefferer, S., 2001. Micromechanical and macromechanical effects in grain scale polycrystal plasticity experimentation and simulation. Acta Mater. 49 (17), 3433–3441.
Rice, J., 1981. Constraints on the diffusive cavitation of isolated grain boundary facets in creeping polycrystals. Acta Metall. 29 (4), 675–681.
Science, N.I.f.M., 2014. Data sheets of the elevated-temperature properties of 9Cr-1Mo-V-Nb steel tubes for boilers and heat exchangers, 9Cr-1Mo-V-Nb steel plates for boilers and pressure vessels and 9Cr-1Mo-V-Nb seamless pipe for high temperature service. In: Proceedings of the NIMS Creep Data Sheet No. 43A. Tsukuba, Japan. NIMS.
Shinozaki, K., Kuroki, H., 2003. Stress-strain analysis of creep deterioration in heat affected weld zone in high Cr ferritic heat resistant steel. Mater. Sci. Technol. 19 (9), 1253–1260.
Smith, D., Walker, N., Kimmins, S., 2003. Type iv creep cavity accumulation and failure in steel welds. Int. J. Press. Vess. Pip. 80 (9), 617–627.
Tabuchi, M., Takahashi, Y., 2006. Evaluation of creep strength reduction factors for welded joints of modified 9Cr-1Mo steel (P91), ASME 2006 pressure vessels and piping/ICPVT-11 conference. Am. Soc. Mech. Eng. 529–534.
Tabuchi, M., Watanabe, T., Kubo, K., Matsui, M., Kinugawa, J., Abe, F., 2001. Creep crack growth behavior in the Haz of weldments of W containing high Cr steel. Int. J. Press. Vess. Pip. 78 (11–12), 779–784.
Tabuchi, M., Hongo, H., Li, Y., Watanabe, T., Takahashi, Y., 2009. Evaluation of microstructures and creep damages in the HAZ of P91 steel weldment. J. Press. Vess. Technol. 131 (2), 021406.
Tvergaard, V., 1984a. Constitutive relations for creep in polycrystals with grain boundary cavitation. Acta Metall. 32 (11), 1977–1990.
Tvergaard, V., 1984b. On the creep constrained diffusive cavitation of grain boundary facets. J. Mech. Phys. Solids 32 (5), 373–393.
Van Der Giessen, E., Tvergaard, V., 1994. Development of final creep failure in polycrystalline aggregates. Acta Metall. Mater. 42 (3), 959–973.
Wang, X., Wang, X., Luo, B., Guo, J., 2018. Analysis of cavity evolution in 9% Cr heat-resistant steel welded joint during creep. Eng. Fract. Mech 202, 394–404.
Watanabe, T., Tabuchi, M., Yamazaki, M., Hongo, H., Tanabe, T. Creep damage evaluation of 9Cr–1Mo–V–Nb steel welded joints showing type IV fracture, Int. J. Press. Vess. Pip. 83(1) (2006) 63–71.
Yaguchi, M., Ogata, T., Sakai, T., 2010. Creep strength of high chromium steels welded parts under multiaxial stress conditions. Int. J. Press. Vess. Pip. 87 (6), 357–364.
Yatomi, M., Tabuchi, M., 2010. Issues relating to numerical modelling of creep crack growth. Eng. Fract. Mech. 77 (15), 3043–3052.

Yu, C.-.H., Huang, C.-.W., Chen, C.-.S., Gao, Y., Hsueh, C.-.H., 2012. Effects of grain boundary heterogeneities on creep fracture studied by rate-dependent cohesive model. Eng. Fract. Mech. 93, 48–64.
Yu, X., Babu, S.S., Terasaki, H., Komizo, Y., Yamamoto, Y., Santella, M.L., 2013a. Correlation of precipitate stability to increased creep resistance of Cr–Mo steel welds. Acta Mater. 61 (6), 2194–2206.
Yu, C.-.H., Huang, C.-.W., Chen, C.-.S., Gao, Y., Hsueh, C.-.H., 2013b. A micromechanics study of competing mechanisms for creep fracture of zirconium diboride polycrystals. J. Eur. Ceram. Soc. 33 (10), 1625–1637.
Yu, C., Bird, M., Huang, C., Chen, C., Gao, Y., White, K., Hsueh, C., 2014. Micromechanics modeling of creep fracture of zirconium diboride–silicon carbide composites at 1400–1700 °C. J. Eur. Ceram. Soc. 34 (16), 4145–4155.
Zhang, Q., Zhang, J., Zhao, P., Huang, Y., Yang, Y., Zhao, Y., 2015. Microstructure of 10% cr martensitic heat-resistant steel welded joints and type IV cracking behavior during creep rupture at 650 C. Mater. Sci. Eng. A 638, 30–37.
Zhao, L., Jing, H., Xu, L., Han, Y., Xiu, J., 2012a. Analysis of creep crack growth behavior of P92 steel welded joint by experiment and numerical simulation. Mater. Sci. Eng. A 558, 119–128.
Zhao, L., Jing, H., Han, Y., Xiu, J., Xu, L., 2012b. Prediction of creep crack growth behavior in ASME P92 steel welded joint. Comput. Mater. Sci. 61, 185–193.